GEOPHYSICS, VOL. 48, NO. 3 (MARCH 1983); P. 331-340, 11 FIGS., 2 TABLES.

DC telluric fields in three dimensions: A refined finite-difference simulation using local integral forms

John F. Hermance*

ABSTRACT

A new finite-difference form is developed for simulating the distortion of telluric fields by 3-D azimuthally symmetric structures. The technique involves a sequence of local integrations of the electric current density crossing closed surfaces surrounding each mesh node. The resulting expressions, which are accurate to second degree everywhere, correctly describe first-order discontinuities in the electric field normal to electrical discontinuities in the interior of the model. Moreover, the new form (a nine-point finite-difference operator) accounts for cross-derivative (e.g., $\partial^2 U/\partial r \partial z$) effects in the region about each node, which can lead to significantly improved accuracy near sharp, localized discontinuities where the anomalous field decays as $1/R^2$ or $1/R^3$ with distance.

Numerical simulations are compared with analytical solutions for two simple models: (1) a circular disk-shaped heterogeneity in a thin sheet; and (2) a sphere imbedded in a homogeneous, infinite medium. The comparison between the analytical and numerical results for both of these models indicates that an accuracy of better than a few percent is not exceptional.

INTRODUCTION

An important class of problems which is often encountered while interpreting the behavior of time-varying telluric and/or magnetotelluric (MT) fields is concerned with the case in which the depth of penetration δ is much greater than the characteristic dimension L of geologic structures under study. In such situations (where $\delta \gg L$), one can assume that they are dealing with the distortion of dc-telluric or galvanic fields and can neglect, to first order, the effects of self and mutual induction over the dimensions of the body considered (Berdichevskiy, 1965; Hermance, 1982a).

Being able to invoke this limiting situation enables one to simulate effectively with numerical models the long-period distortion of telluric fields in the vicinity of surficial lateral heterogeneities. Such shallow geologic structures may or may not be of direct interest in a specific exploration program. However, there is little doubt that galvanic effects can appreciably perturb the long-period MT response of such a structure, even when its induction parameter (L/δ) is negligible (Berdichevskiy and Dmitriev, 1976; Hermance, 1982a). Hence we adopt the point of view that while at present there is limited interest among exploration geophysicists in quantitatively interpreting the results of telluric surveys, the effects of phenomena associated with telluric field distortion can significantly modify the MT response at long periods and thus lead to strongly biased interpretations if not properly accounted for (Hermance, 1982a). Therefore this paper, while restricted to considering the dc-telluric case, lays the foundation for addressing a larger range of problems commonly encountered in conventional MT surveys.

We are concerned with developing an accurate numerical algorithm which adequately accounts for the physical behavior of electric fields in the vicinity of sharp electrical discontinuities within the interior of our modeling region. The technique involves the extension to three dimensions of the concept of local integral forms developed by Hermance (1982b) for two dimensions. As shown in this previous work, the method is quite similar to the finite-difference technique although a somewhat higher accuracy is to be expected, particularly in the vicinity of electrical discontinuities where the perturbed fields decrease rapidly with distance. In simulating such models, the problem reduces to the analog of solving Laplace's equation for a scalar potential field. This not only simplifies the mathematics in deriving the appropriate numerical algorithm, it also reduces computation times on a computer dramatically, particularly when certain symmetries in the model are exploited.

THE MODEL

The class of models considered here is limited to azimuthally symmetric structures (an example is illustrated in Figure 1). The resistivity structure can vary arbitrarily in the radial or vertical direction, but it is constrained to be symmetric in the azimuthal plane. Although the geometry is somewhat restrictive, such models can be used to represent circular basins, domes, laccoliths, hydrothermal plumes, ocean islands, etc. At this point I feel that there are decided advantages to employing this symmetry: first, it is possible quantitatively to compare the results of the numerical model with those from analytical models which have cylindrical or spherical symmetry; second, the computation time is reduced appreciably. As will be shown below, the problem effectively

Manuscript received by the Editor October 6, 1981; revised manuscript received June 23, 1982.
*Geophysical/Electromagnetic Laboratory, Department of Geological Sciences, Brown University, Providence, RI 02912.

reduces from evaluating fields at the nodes of a 3-D mesh to evaluating the fields at the nodes of a 2-D mesh which has rotational symmetry about the center of the structure. The reader should readily perceive the straightforward application of these concepts to more general cases.

The method begins with a global discretization of the model over the region of interest, as is usually done in conventional finite differences (e.g., Mufti, 1976; Dey and Morrison, 1979a, b). We then perform a local surface integration of the electric field in the vicinity of each grid node. The method is described for 2-D structures by Hermance (1982b), where it is shown that although the resulting simulation has the form of a nine-point finite-difference expression, it has a higher precision than the more conventional five-point finite-difference forms.

Basic theory

The discussion follows the theory presented by Hermance (1982b) and only some of the essential relations are reviewed here. Upon invoking the low-frequency or dc approximation and neglecting the contribution from any frequency-dependent induction phenomena, the electrical field can be represented by the gradient of a scalar potential, e.g.,

$$\mathbf{E} = -\nabla U, \tag{1}$$

where U is a solution to Laplace's equation

$$\nabla^2 U = 0. \tag{2}$$

An alternative approach would be to use the continuity con-

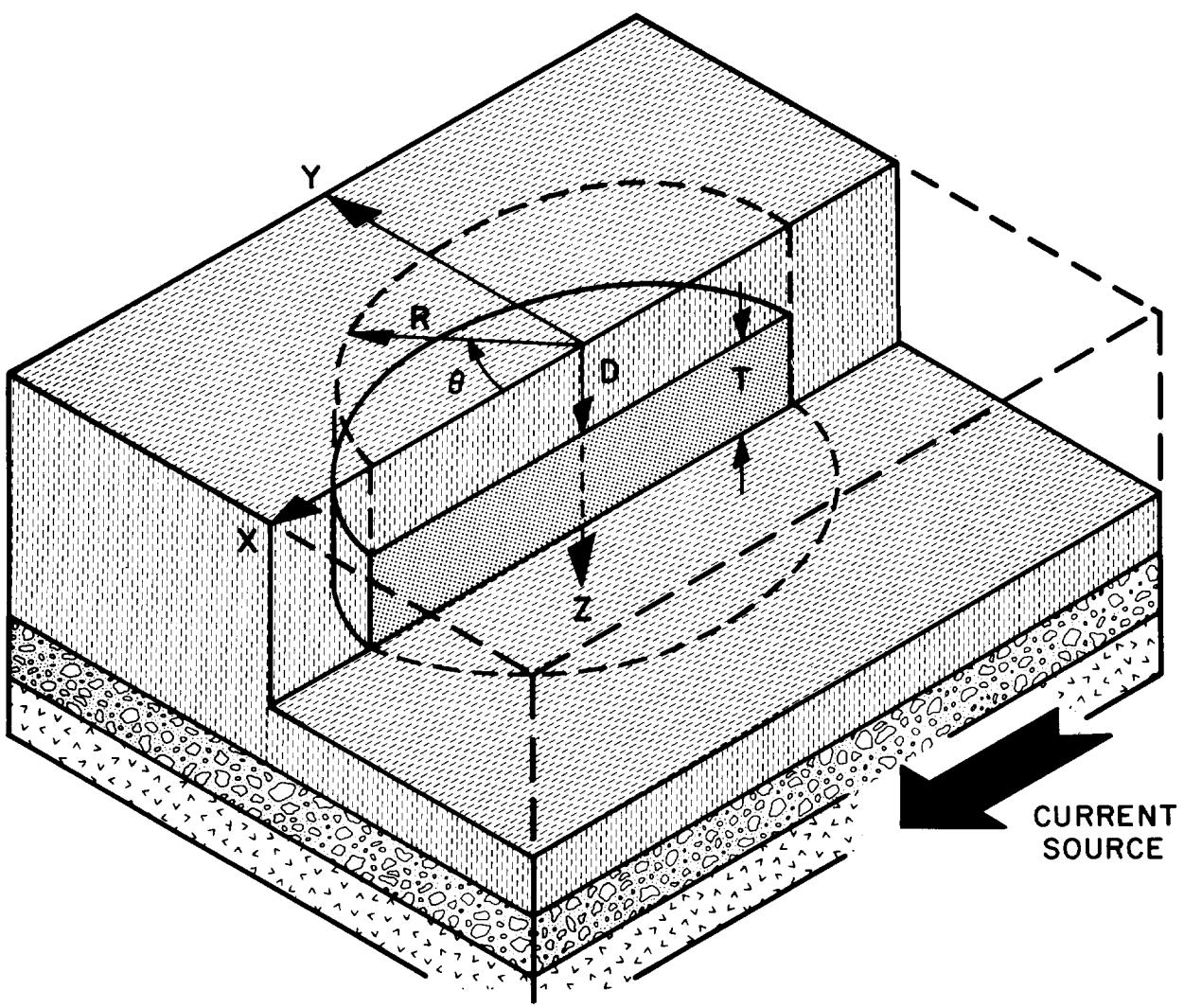

FIG. 1. An example of the type of azimuthally symmetric 3-D model to be considered. The heterogeneity need not be imbedded in a homogeneous layer, but it can simulate a local geometrical modulation (thinning or thickening) of a surface layer or a layer at depth. The conventions of the x, y, z and r, θ, z coordinate systems are shown relative to an origin over the center of the heterogeneity.

dition on the electric current density,

$$\nabla \cdot (\mathbf{J} + \partial \mathbf{D}/\partial t) = 0, \tag{3}$$

$\mathbf{J}$ being the conduction current density (A/m^2), and $\partial \mathbf{D}/\partial t$ the displacement current density (A/m^2). Since frequency and time-dependent effects are neglible, we set the time derivatives of all variables to zero. Hence

$$\nabla \cdot \mathbf{J} = 0, \tag{4}$$

which, because of Ohm's law in point form ($\mathbf{J} = \sigma \mathbf{E}$), can be related in a homogeneous medium to the divergence of the gradient of a scalar potential as in equation (1) such that one arrives at an expression identical to equation (2).

The conventional finite-difference method is applied by superimposing an irregularly spaced grid on the region containing the structure to be studied. This forms a basis for a coordinate system, with the spacing between grid lines usually arranged so that the mesh is small near where fields are expected to vary significantly over small distances, i.e., near the boundaries of structures. Relations such as (2) or (4) are then sought for each nodal point P throughout the grid mesh.

As outlined by Hermance (1982b), the fundamental concept underlying the new tecnique is the fact that the differential form (4) is not the most primitive form of Maxwell's equations. Integral forms are more basic. Therefore, an appropriate integration of field quantities is invoked in the vicinity of each of the grid nodes which, in the case of telluric or dc fields, involves the conservation of current expressed by

$$\iint J \cdot dA = 0, \tag{5}$$

where the surface integration totally encloses a particular grid node P. The objective is to perform the required surface integration to second-degree accuracy in the vicinity of each nodal point over the interior of the model.

Basic conventions

For azimuthally symmetric structures, the model can be described completely by specifying values for the resistivity over a single mesh in the r, z plane at $\theta = 0$. A simple rotation of the mesh from $\theta = 0$ to 360 degrees will then trace out the actual structure. In this case, it is apparent that the most complicated boundary to be encountered in the vicinity of any node P is when four dissimilar materials abut along a line in the θ direction, as shown in Figure 2.

The convention for describing the nodes which are the nearest neighbors of P is indicated in Figure 3. The contact, or central point (actually a line in the θ direction) at which nodal planes

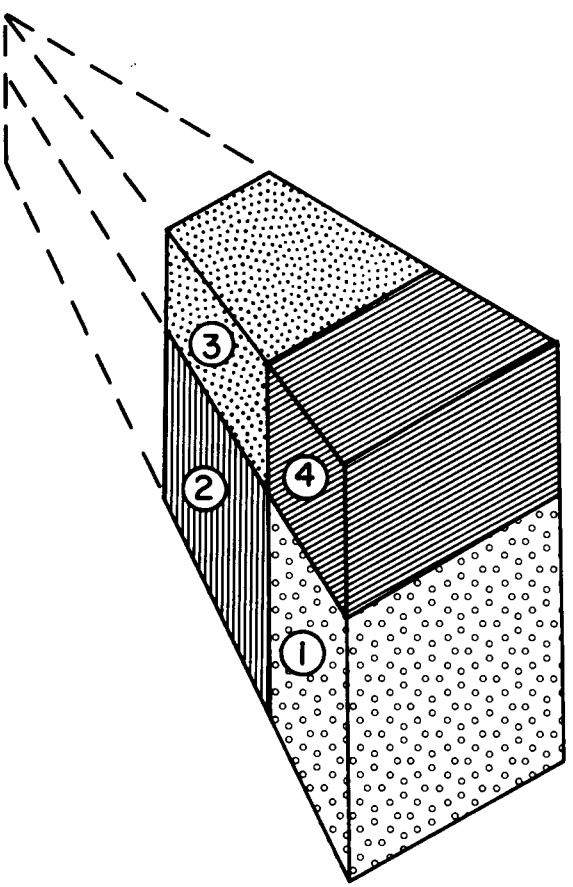

FIG. 2. A local segment of the model showing the most pathologic situation to be encountered in the vicinity of a grid node at the interface of an electrical discontinuity; four dissimilar materials abutting along a line in the θ direction.

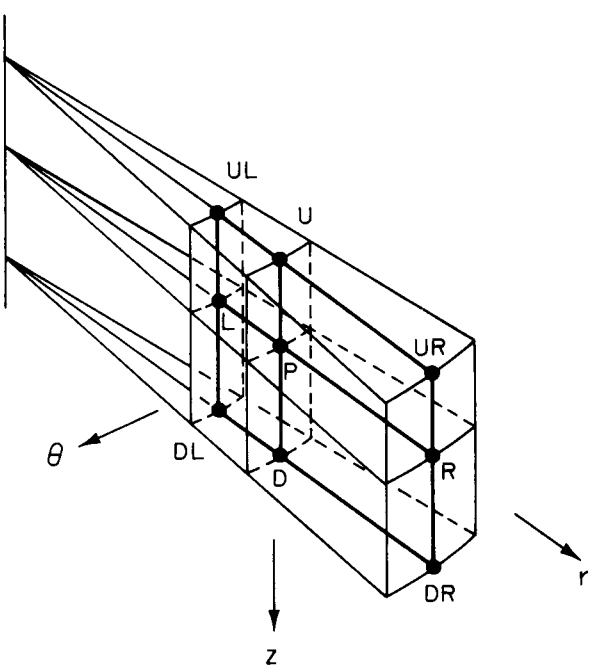

FIG. 3. The notation used to describe the coupling of eight neighboring nodes to the central node P. The letters UR denote upper-right, DR denote down-right, etc. The width of the segment in the azimuthal direction, $\Delta\theta_w$, is considered to be arbitrarily small.

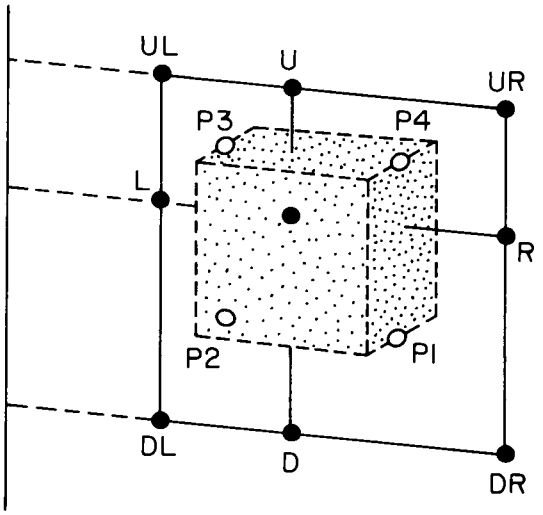

FIG. 4. The surface over which the normal current density is to be integrated. Note the temporary nodes $P1$, $P2$, $P3$, and $P4$ which are introduced at the midpoint of each surrounding prism and which describe the edges of the enclosed volume.

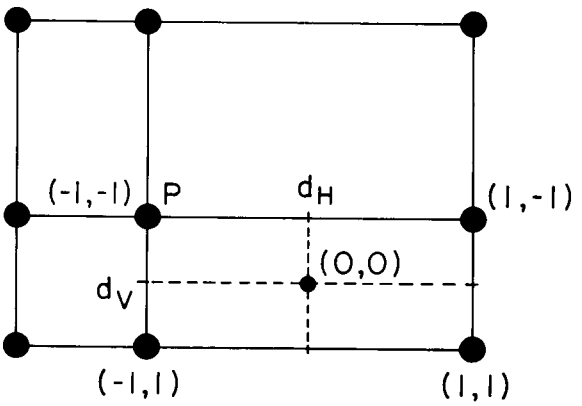

FIG. 5. Notation used to express the local coupling relations at the temporary node (0, 0). Each of the four regions about P has a similar geometry, although for clarity these are not shown.

come into contact, is labeled P, and the grid surfaces delineate four quasi-rectangular prisms, labeled 1 through 4 (see Figure 2), each possibly having a different value of conductivity σ_j (or its inverse, resistivity ρ_j), where the index $j = 1$ to 4 corresponds to the respective medium. These prisms each have nodal points at their corners (Figure 3); R signifies right, D down, L left, and U up. It follows that the label UR denotes upper right, etc. The spacings between the central node P and its nearest neighbors R, D, L, and U are given, respectively, by d_R, d_D, d_L, and d_U. The width of each prism in the azimuthal direction is $\Delta\theta_w$, which we assume is a small angle.

Surface integration of normal current density

Local Taylor series representations.—The surface of integration for the normal current density is shown in Figure 4. A set of temporary nodes, one at the center of each rectangular region, is labeled P1, P2, P3, and P4. The potential field U_j in each medium can be locally represented as a second-degree polynomial form relative to a coordinate system centered at P1, P2, P3, or P4, respectively. It follows, therefore, that a local Taylor series expansion of U_j can be developed for each medium (1 through 4) about the temporary points P1 through P4, respectively. The form of such an expansion is

$$\begin{aligned} U_J = {} & U_{Pj} + \Delta r\, \partial U/\partial r|_{Pj} + \Delta\theta\, \partial U/\partial\theta|_{Pj} + \Delta z\, \partial U/\partial z|_{Pj} \\ & + \Delta r\Delta\theta\, \partial^2 U/\partial r\partial\theta|_{Pj} + \Delta z\Delta\theta\, \partial^2 U/\partial z\partial\theta|_{Pj} \\ & + \Delta r\Delta z\, \partial^2 U/\partial r\partial z|_{Pj} + (\Delta r^2/2)\partial^2 U/\partial r^2|_{Pj} \\ & + (\Delta\theta^2/2)\partial^2 U/\partial\theta^2|_{Pj} + (\Delta z^2/2)\partial^2 U/\partial z^2|_{Pj}, \end{aligned} \tag{6}$$

where $\Delta r = r - r_{Pj}$, $\Delta\theta = \theta - \theta_{Pj}$, and $\Delta z = z - z_{Pj}$ are distances referenced to a set of local coordinate systems, each having its origin at the center of a rectangular region such as shown in Figure 5 where, as an example, $j = 1$. In this local region, the origin is designated by the indices (0, 0), the node to the right and down by (1, 1), the node to the left and down by (−1, 1), etc. Note that these integers are not distances, but indices. The distance between nodes is d_H in the horizontal direction and d_V in the vertical direction.

The continuous derivatives evaluated at each of the temporary nodes can be approximated by the following centered difference operators which are accurate to second degree (see Hermance, 1982b):

$$\begin{aligned} [\partial U/\partial r]_j &\cong D_{rj}(U) \\ &= [U_j(1, 1) + U_j(1, -1) - U_j(-1, 1) \\ &\quad - U_j(-1, -1)]/2d_H. \end{aligned} \tag{7}$$

$$\begin{aligned} [\partial U/\partial z]_j &\cong D_{zj}(U) \\ &= [U_j(1, 1) + U_j(-1, 1) - U_j(1, -1) \\ &\quad - U_j(-1, -1)]/2d_V. \end{aligned} \tag{8}$$

$$\begin{aligned} [\partial^2 U/\partial r\partial z]_j &\cong D_{rzj}(U) \\ &= \{[U_j(1, 1) - U_j(-1, 1)]/d_H \\ &\quad - [U_j(1, -1) - U_j(-1, -1)]/d_H\}/d_V. \end{aligned} \tag{9}$$

An operator denoted by the upper case D represents one of the finite-difference forms in equations (7), (8), or (9).

It is useful to recognize at this point that the potential field is continuous across the four interfaces separating the various media, whereas its first and second derivatives with respect to r and z may be discontinuous. On the other hand, because of the azimuthal symmetry of the structure, the first and second derivatives of U with respect to θ are continuous across all interfaces.

The function U can be expanded as a Fourier series in θ such that

$$U(r, z, \theta) = \sum_{n=0}^{\infty} U_n(r, z) \exp(in\,\theta), \tag{10}$$

where $U_n(r, z)$ is generally complex and depends upon the order n of the Fourier term. For electric field sources which are spatially uniform and polarized in the x-direction, equation (10) reduces to

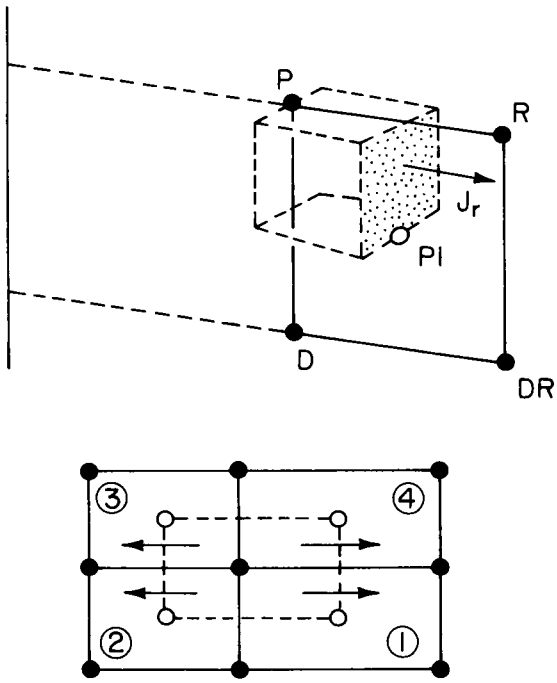

FIG. 6. Top: illustrates the integration of the normal current density J_r over the surface $r = r_{P1}$ in medium 1. Bottom: illustrates the convention for integrating J_r over all the appropriate surfaces in media 1, 2, 3, and 4.

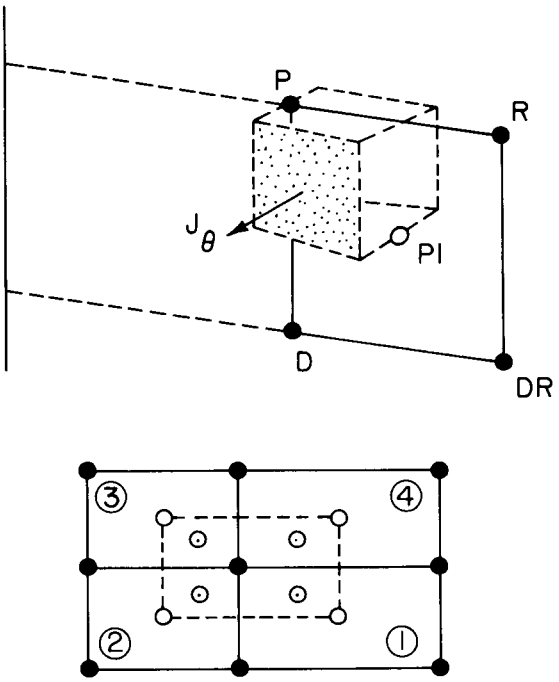

FIG. 7. Top: illustrates the integration of the normal current density J_θ over the surface $+\Delta\theta_w/2$. Bottom: illustrates the convention for integrating J_θ over all the appropriate surfaces in media 1, 2, 3, and 4. The encircled point represents the tip of an arrow directed toward the reader.

$$U(r, z, \theta) = U(r, z) \cos \theta, \tag{11}$$

where $U(r, z)$ is purely real. It is convenient for future applications of the model to consider the more general Fourier term represented by equation (10) so that upon suppressing the summation sign

$$U(r, z, \theta) = U_n(r, z) \exp(in\,\theta) \tag{12}$$

along with the derivatives

$$\partial U/\partial\theta = in\,U, \tag{13}$$

and

$$\partial^2 U/\partial\theta^2 = -n^2\,U. \tag{14}$$

The electric field components in the jth medium are given by

$$\begin{aligned} E_{rj} &= -\partial U/\partial r \\ &= -[D_{rj}(U) + (\Delta\theta)in\,D_{rj}(U) \\ &\quad + \Delta z\,D_{rzj}(U) + \Delta r\,\partial^2 U/\partial r^2], \end{aligned} \tag{15}$$

$$\begin{aligned} E_{\theta j} &= -(1/r)\partial U/\partial\theta \\ &= -[(1/r)in\,U_{Pj} + (\Delta r/r)in\,D_{rj}(U) \\ &\quad + (\Delta z/r)in\,D_{zj}(U) - (\Delta\theta/r)n^2 U_{Pj}], \end{aligned} \tag{16}$$

and

$$\begin{aligned} E_{zj} &= -\partial U/\partial z \\ &= -[D_{zj}(U) + in\,\Delta\theta\,D_{zj}(U) \\ &\quad + \Delta r\,D_{rzj}(U) + \Delta z\,\partial^2 U/\partial z^2]. \end{aligned} \tag{17}$$

The surface integration.—Now incorporate expressions (15) through (17) for the electric field components into Ohm's law for each medium, $\mathbf{J}_j = \sigma_j \mathbf{E}_j$, to determine relations for the appropriate components of the normal current density. These can then be integrated over the surface of the volume indicated in Figure 4. Begin by integrating J_r over the surface in medium 1, at constant radius $r = r_{P1}$, as shown in the top diagram of Figure 6. The total current passing radially outward through this surface is given by

$$I_{rP1} = -(\sigma_1 r_{P1}\Delta\theta_w\,d_D/2)[D_{r1}(U) - (d_D/4)D_{rz1}(U)], \tag{18}$$

where $\Delta\theta_w$, the angular width of the volume, is assumed to be arbitrarily small.

In a similar way the total current passing outward through each of the other surfaces shown in the lower diagram of Figure 6 is given, respectively, by

$$I_{rP2} = +(\sigma_2 r_{P2}\Delta\theta_w\,d_D/2)[D_{r2}(U) - (d_D/4)D_{rz2}(U)], \tag{19}$$

$$I_{rP3} = +(\sigma_3 r_{P3}\Delta\theta_w\,d_U/2)[D_{r3}(U) + (d_U/4)D_{rz3}(U)], \tag{20}$$

and

$$I_{rP4} = -(\sigma_4 r_{P4}\Delta\theta_w\,d_U/2)[D_{r4}(U) + (d_U/4)D_{rz4}(U)]. \tag{21}$$

Another set of surfaces is shown in Figure 7 over which J_θ is integrated. It is most useful to consider the sum of the integrated current passing through a surface at $+\Delta\theta_w/2$ and that passing through another surface at $-\Delta\theta_w/2$, where $\Delta\theta_w$ is small. In this case the sum of currents passing outward through these two

surfaces in medium 1 is

$$\Delta I_{\theta P1} = -\int_{r_p}^{r_p + d_R/2} \int_0^{d_D/2} [(\sigma_1 \Delta\theta_W / r)\, \partial^2 U/\partial\theta^2]\, dz\, dr. \quad (22)$$

Upon noting that $\partial^2 U/\partial\theta^2 = -n^2 U$, equation (22) can be numerically integrated using the trapezoidal rule. To do so, the convention for indices shown in Figure 5 to identify the position of each node (or temporary node) is employed. Hence, performing the surface integration in (22) using the 2-D trapezoidal formula leads to

$$\Delta I_{\theta P1} = (\sigma_1\, d_D d_R\, \Delta\theta_W n^2/16)[U(-1, -1)/r_p + U(0, -1)/r_{P1} + U(0, 0)/r_{P1} + U(-1, 0)/r_p]. \quad (23)$$

Since permanent nodes are not associated with the positions $(0, -1)$, $(0, 0)$, and $(-1, 0)$, the potential at these points is determined using the Taylor series expansion given in equation (6), where the derivatives are given by equations (7), (8), and (9). For example, expanding about the temporary node $P1$ [corresponding to position $(0, 0)$] leads to the following relation for the potential at node P:

$$U_P = U_{P1} - (d_R/2)D_{r1}(U) - (d_D/2)D_{z1}(U) + (d_R d_D/4)D_{rz1}(U). \quad (24)$$

This can be rewritten in the form

$$U_{P1} = U_P + (d_R/2)D_{r1}(U) + (d_D/2)D_{z1}(U) - (d_R d_D/4)D_{rz1}(U). \quad (25)$$

Equation (25) is an expression for U_{P1} [or $U(0, 0)$] in terms of the potential at its nearest neighbor nodes. In a similar way one can solve for the potential at the other temporary nodes [$(0, -1)$ and $(-1, 0)$]. Following some straightforward algebra, one finds that equation (23) can be expanded to the form

$$\Delta I_{\theta P1} = (\sigma_1\, d_D d_R\, \Delta\theta_W n^2/16) \cdot [U_P/r_P + (U_P + U_R)2r_{P1} + (U_P + U_D)/2r_p + (U_P + U_R + U_{DR} + U_D)/4r_{P1}]. \quad (26)$$

Integrating over the other surfaces shown in Figure 7 leads to the following expressions for the differential currents (i.e., the difference between the azimuthal current passing outward through the surface at $+\Delta\theta_W/2$ and that passing inward through the surface at $-\Delta\theta_W/2$ in each medium):

$$\Delta I_{\theta P2} = (\sigma_2\, d_D d_L\, \Delta\theta_W n^2/16)[U_P/r_p + (U_P + U_L)/2r_{P2} + (U_P + U_D)/2r_p + (U_P + U_L + U_{DL} + U_D)/4r_{P2}], \quad (27)$$

$$\Delta I_{\theta P3} = (\sigma_3\, d_U d_L\, \Delta\theta_W n^2/16)[U_P/r_p + (U_p + U_L)/2r_{P3} + (U_P + U_U)/2r_p + (U_P + U_L + U_{UL} + U_U)/4r_{P3}], \quad (28)$$

and

$$\Delta I_{\theta P4} = (\sigma_4\, d_U d_R\, \Delta\theta_W n^2/16)[U_P/r_p + (U_P + U_R)/2r_{P4} + (U_P + U_U)/2r_p + (U_P + U_U + U_{UR} + U_R)/4_{r4}]. \quad (29)$$

Finally, consider the vertical current density passing through the surfaces indicated in Figure 8. The total integrated current passing through the surface in medium 1 containing the point $P1$ is

$$I_{zP1} = -(\sigma_1 r_P \Delta\theta_W\, d_R/2)(D_{z1}(U)[1 + (d_R/4r_P)] - D_{rz1}(U)\{(d_R/4)[1 + (d_R/6r_P)]\}). \quad (30)$$

The total integrated current densities passing outward through each of the other surfaces in Figure 8 are given, respectively, by

$$I_{zP2} = -(\sigma_2 r_P \Delta\theta_W\, d_L/2)(D_{z2}(U)[1 - (d_L/4r_p)] + D_{rz2}(U)\{(d_L/4)[1 - (d_L/6r_p)]\}), \quad (31)$$

$$I_{zP3} = +(\sigma_3 r_P \Delta\theta_W\, d_L/2)\{D_{z3}(U)[1 - (d_L/4r_P)] + D_{rz3}(U)[(d_L/4)[1 - (d_L/6r_P)]\}), \quad (32)$$

and

$$I_{zP4} = +(\sigma_4 r_P \Delta\theta_W\, d_R/2)(D_{z4}(U)[1 + (d_R/4r_P)] - D_{rz4}(U)\{(d_R/4)[1 + (d_R/6r_P)]\}). \quad (33)$$

Clearly the total current passing outward through the entire closed surface indicated in Figure 4 is simply the sum of the right-hand sides of expressions (18) through (21), (26) through (29), and (30) through (33), inclusive. The resulting expression, after eliminating the constant multiplier $\Delta\theta_W/2$, becomes the desired numerical operator. It is easy to show that as r_p becomes large relative to the nodal spacing, the above expression reduces to the 2-D finite-difference form described by Hermance (1982b).

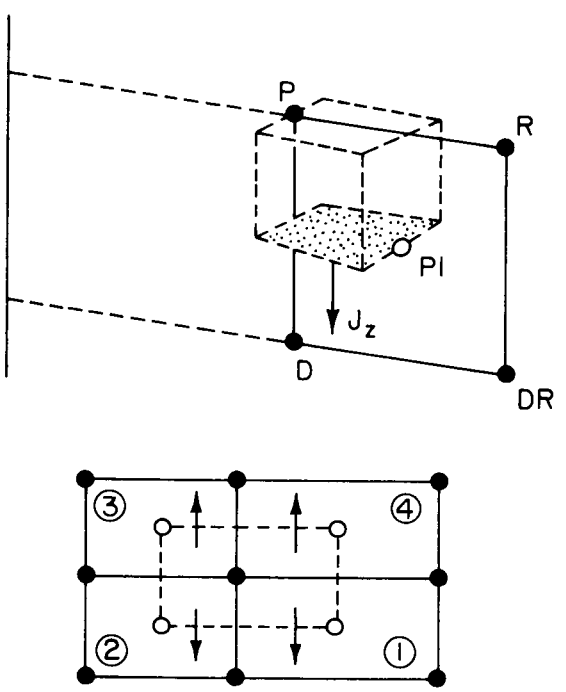

FIG. 8. Top: illustrates the integration of the normal current density J_z over the surface at $z = d_R/2$ below the point P in medium 1. Bottom: illustrates the convention for integrating J_z over all the appropriate surfaces in media 1, 2, 3, and 4.

COMPARISON OF NUMERICAL AND ANALYTICAL RESULTS FOR SIMPLE MODELS

Circular disk in a thin sheet

An important test for evaluating the modeling algorithm is to see if it can simulate the distortion of electric fields in the vicinity of a circular disk-shaped heterogeneity in a thin sheet (Figure 9). This problem is readily evaluated analytically and represents a simple member of the class of problems where geologic heterogeneities outcrop at the surface.

The electric potential was calculated for a set of 25 nodes un-

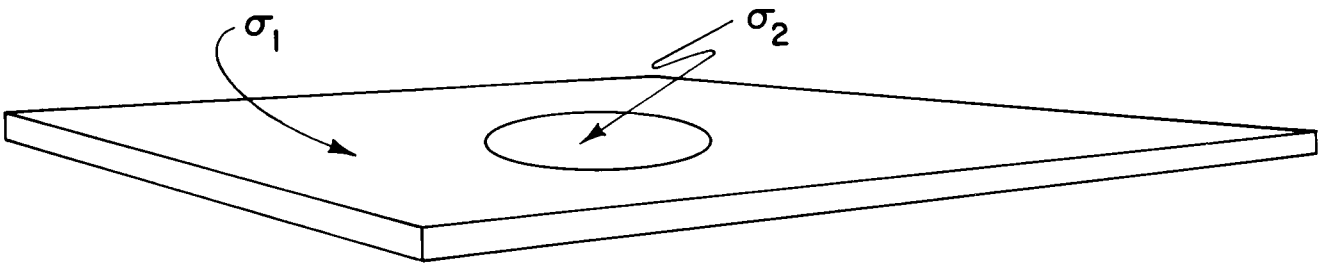

FIG. 9. A circular disk-shaped heterogeneity in a thin sheet.

equally spaced from the center of a disk having a radius R_d = 100 m, to a distance of 1000 m (10 R_d). The thin sheet was 10 m thick over which 5 vertical nodes were equally spaced at distances of 2.5 m. A boundary condition of $E_z = 0$ was imposed along the top and bottom horizontal surfaces. At the origin $U = 0$, whereas at infinity (r = 10 R_d) a constant gradient was imposed simulating a uniform source field of

$$E_x(\text{source}) = 1.0 \text{ V/m}. \tag{34}$$

At each internal node the local integration described in the previous section was applied, leading to a set of coupled linear equations in the unknown potentials. In the present code double precision variables were used (16 significant figures in floating point form) and the arrangement of the finite-difference expressions was ordered in such a way that a strongly banded (bandwidth = twice the number of horizontal nodes + 3), diagonally dominant matrix was generated. For small models (25 × 25 nodes), this type of matrix is quite suitable for inversion by Gauss elimination; pivoting is not required, the elimination is performed only on the band containing nonzero coefficients, and the matrix inversion is quite stable.

The electric field components are determined from the discretized potential field solutions using modified centered difference gradient operators (see the Appendix). The electric field **E** therefore is a derived quantity; it is not a primary quantity, such as U_P which is calculated during the original numerical simulation. One might expect some loss of precision to occur at this secondary level of calculation. A third level of calculation (and associated imprecision) is introduced when the results are cast in terms which are most useful to the exploration geophysicist, who is interested in the anomalous electric field relative to the source field, i.e.,

$$\Delta E_x = [E_x(x) - E_x(\text{source})]/E_x(\text{source}). \tag{35}$$

This residual quantity is due solely to the effects of the electrical heterogeneity, and its numerical evaluation tends to emphasize any imprecision in the model calculation.

The results of the numerical simulation of the circular disk-shaped heterogenetity in a thin sheet are summarized in Figure 10. Also shown is the analytical solution to the same problem. The anomalous horizontal electric field component given by equation (35) is presented at points along a radial profile from the center of the disk parallel to the direction of the source field, E_x (source). We plotted our results in logarithmic coordinates to emphasize the $1/R^2$ decrease of the anomalous field with distance beyond the edge of the disk. Another feature of the result is the typically constant value of the electric field over the interior of the disk, given analytically by

$$\Delta E_x = -(\sigma_2 - \sigma_1)/(\sigma_2 + \sigma_1). \tag{36}$$

In the case shown here, where σ_1 = 0.1 S/m and σ_2 = 1.0 S/m, ΔE_x = 0.82, with which the numerical results agree quite well (see Figure 10 and Table 1).

It is important to recognize that the anomalous electric field is not continuous across the edge of the disk, but undergoes a discontinuity associated with a change in sign. Since such a change in sign cannot be shown directly in logarithmic coordinates, we have indicated this implicitly with the negative sign (−) and positive sign (+) in brackets. When σ_2(disk) > σ_1(sheet), the anomalous field is negative over the interior of the disk and positive beyond the disk. Hence the anomalous electric field is

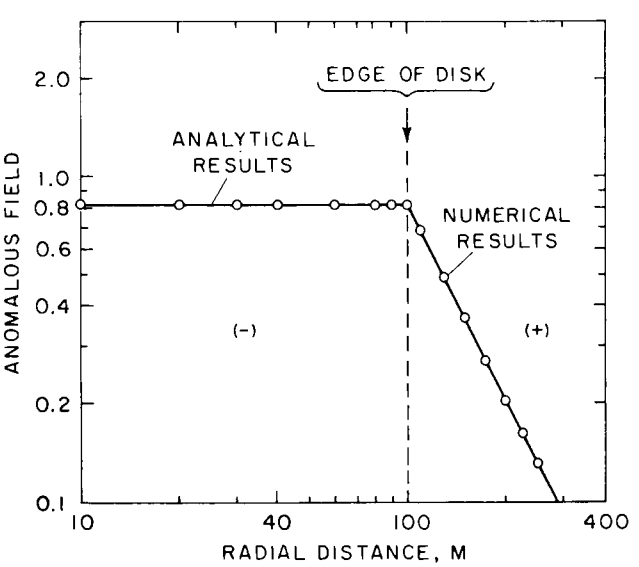

FIG. 10. Comparison of analytical (solid line) and numerical results (points) for the anomalous electric field due to a circular disk-shaped heterogeneity in a thin sheet; σ_1(sheet) = 0.1 mho/m and σ_2 = 1.0 mho/m.

Table 1. Comparison of numerical and analytical results for a disk-shaped heterogeneity in a thin sheet. Radius a of disk = 100 m, conductivity of disk = 1 mho/m, conductivity of host medium = 0.1 mho/m.

	Anomalous field		
Distance(m)	Numerical	Analytical	Normalized error (%)
0.	−.820	−.818	0.2
10.	−.820	−.818	0.2
20.	−.820	−.818	0.2
30.	−.820	−.818	0.2
40.	−.820	−.818	0.2
60.	−.820	−.818	0.2
80.	−.820	−.818	0.2
90.	−.820	−.818	0.2
100.(−)*	−.819	−.818	0.1
100.(+)**	+.809	+.818	−1.1
110.	+.670	+.676	−0.9
130.	+.480	+.484	−0.8
150.	+.358	+.364	−1.6
		rms error	0.6%

*Denotes the horizontal electric field is evaluated at $r < a$, but immediately adjacent to discontinuity.
**Denotes the field is evaluated at $r > a$, but immediately adjacent to discontinuity.

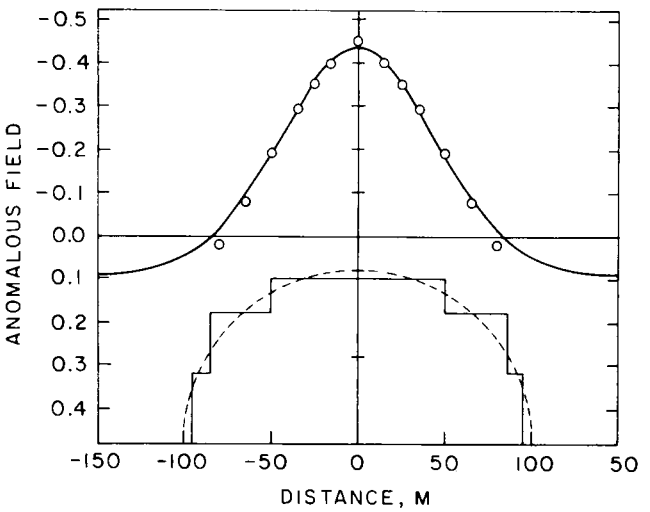

FIG. 11. Comparison of analytical (solid line) and numerical results (points) for the anomalous electric field due to a sphere imbedded in an infinite homogeneous medium; σ_1(host) = 0.1 mho/m, σ_2(sphere) = 1.0 mho/m. The height of the profile is −120 m above the center of a sphere having a radius of 100 m. The spherical heterogeneity is approximated by an equal volume set of cylindrical structures as shown in vertical section. The radius of the points is approximately 2 percent of the maximum analytic field value.

not continuous across the edge of the disk as it may first appear from Figure 10.

Although the numerical and analytical results shown for this model in Figure 10 seem to agree quite well, a better idea of the overall distribution of errors may be obtained from a close inspection of Table 1. Here we indicate, for a few representative points, the results of the numerical calculation, the analytical solution, as well as the difference between the two, as given by

$$R_N = [\Delta E_x(\text{numer.}) - \Delta E_x(\text{analyt.})]/\Delta E_x(\text{analyt.}), \quad (37)$$

expressed as a percentage. This table also summarizes the root-mean-square (rms) value of all the normalized residuals of the numerical result, which is calculated by taking the square root of the mean of the normalized residuals squared.

This comparison should dispell any notion that numerical model studies are intrinsically inaccurate. We should emphasize again that we are at the third level of imprecision in the calculation; the agreement between the primary field quantities, the electric potentials U calculated directly in the numerical simulation, is even more striking.

An imbedded sphere

In this section analytical and numerical calculations for a sphere in a homogeneous medium are compared. Neither calculation accounts for the effects of the earth's surface.

The model consists of 30 × 30 nodes unequally spaced radially from $r = 0$ to 1500 m and vertically from $z = 0$ to −1500 m. A spherical-shaped inclusion is simulated numerically by a set of discrete cylindrical-shaped structures centered at the origin $(r, z) = (0, 0)$ as shown in Figure 11. The total volume of the cylinders is set equal to the volume of a sphere having a radius (R_s) of 100 m. A symmetric boundary condition is applied along the bottom-most plane. It is important to note, of course, that one cannot expect complete agreement between the numerical and analytical results in this case because of the higher order multipole moments which are induced in the cylindrical-shaped structure which are not present in the analytical sphere. The induced field in the analytical calculation is simply that of a dipole. However, one feels intuitively that if the sphere is represented by a set of cylinders as shown, and if one is not too close to the anomalous structure, then certainly the induced dipole terms in the numerical solution should dominate the higher order multipole terms. This seems to be the case as illustrated in Figure 11, where the results are presented for the anomalous horizontal electric field component along a radial profile parallel to the source field at a height of −110 m (where R_s = 100 m).

In an actual field survey, explorationists would tend to extract two pieces of information from such a profile: the peak anomaly and the half-width of the anomaly. What is apparent in this figure, as well as in Table 2, is that the numerical simulation of both parameters is in excellent agreement with the analytical solution over the most critical portions of the profile. However, it is clear in Table 2 that the normalized residuals, as determined using equation (37), are not always a good measure of the overall precision of the data, particularly when the anomalous field amplitudes become very small. Because of this it is useful to introduce a parameter which normalizes the difference between the numerical simulation and the analytical calculation in a somewhat different fashion. Rather than dividing this difference by the analytical value at the same point as is done in equation (37), an alternative approach is to divide the difference by the strength of the source field, i.e.,

$$R_N^S = [\Delta E_x(\text{numer.}) - \Delta E_x(\text{analyt.})]/E_x^0. \quad (38)$$

As seen in Table 2, this leads to much more stable values of the normalized residual. Which of these normalization procedures is to be preferred depends upon the exact application. If an interpretation depends heavily on determining the peak amplitude, the

Table 2. Numerical and analytical results for a sphere imbedded in a homogeneous medium. Height of profile = −110 m, radius of sphere = 100 m, conductivity of sphere = 100 mho/m, conductivity of host medium = 0.1 mho/m.

Anomalous field			Percent error (%)	
Distance (m)	Numerical	Analytical	Normalized by corresponding analytical value	Normalized by source field strength
0.	−0.570	−0.563	1.2	0.7
5.	−0.561	−0.558	0.5	0.3
10.	−0.540	−0.543	−0.5	−0.3
20.	−0.490	−0.485	1.0	0.5
30.	−0.420	−0.401	4.7	1.9
35.	−0.371	−0.353	8.2	1.8
40.	−0.318	−0.304	4.6	1.4
50.	−0.216	−0.207	4.4	0.9
58.	−0.141	−0.135	4.4	0.7
65.	−0.086	−0.080	7.5	0.6
75.	−0.022	−0.015	47.	0.7
80.	−0.004	−0.011	64.	−0.7
90.	−0.043	−0.053	20.	−1.0
101.	−0.074	−0.084	12.	−1.0
110.	−0.091	−0.100	9.0	−1.0
120.	−0.103	−0.110	6.4	−0.7
135.	−0.111	−0.114	2.6	−0.3
150.	−0.111	−0.111	0.0	0.0

geometric half-width and perhaps the total area under the curve, then probably equation (38) is a proper measure of the overall accuracy of the numerical results. On the other hand, if one wants to extract second-order parameters from the model, then equation (37) is useful for indicating those segments of the profile where such a procedure may be misleading.

DISCUSSION

Significant developments have been made over the last decade in numerically modeling geophysically relevant three-dimensional (3-D) problems (Jones and Pascoe, 1972; Raiche, 1974; Weidelt, 1975; Hohmann, 1975; Reddy et al 1977). However, for the most part these techniques have only been used to describe the response of locally imbedded features such as cubes or rectangular prisms (Jones, 1974; Reddy et al, 1977; Wannamaker et al, 1980; Ting and Hohmann, 1980), geometries which cannot be directly compared with analytical results. I have attempted to ameloriate this situation to some degree by considering geometries which have analytical counterparts. In addition, while developing the present algorithm I have paid close attention to having the field relations obey basic physical principles at nodes which are located along internal discontinuities in the electrical conductivity (i.e., where normal-**E** is discontinuous). Moreover, the algorithm I have described is accurate to second degree not only in homogeneous regions, but also in regions closely adjacent to physical discontinuities. The numerical operator incorporates explicit forms for the cross-derivatives which may be essential for most accurately reconstructing the distortion of fields near localized discontinuities [see Hermance (1982b) where this is discussed in detail for two dimensions]. Upon comparing the numerical simulation with analytical calculations for simple models where the expected results are well-known, one sees that accuracies better than a few percent are not exceptional.

I emphasize that the present code does not account for induction effects, which should clearly dominate the actual results when penetration depths δ become less than some characteristic dimension L of the model. This is a profound handicap in the application of the algorithm to conventional MT surveys over a broad range of frequencies. However, in many cases, one is interested in analyzing the effects of 3-D structures when $\delta/L \gg 1$, i.e., at the long-period asymptotic limit. In such cases Hermance (1982a) has shown how the telluric response function can be cast in terms of MT response parameters. Such an approach would be useful for interpreting long-period data from telluric-magnetotelluric surveys as described by Hermance and Thayer (1975), providing one follows the cautionary notes recently discussed by Stodt et al (1981).

ACKNOWLEDGMENTS

The preparation of this manuscript was supported under contract no. DE-AC02-79ER10401 from the Dept. of Energy Office of Basic Energy Sciences.

REFERENCES

Berdichevskiy, M. N., 1965, Electrical prospecting with the telluric current method: Quart. Colo. School Mines, v. 60, no. 1, 216 p.

Berdichevskiy, M. N., and Dmitriev, I. I., 1976, Basic principles of interpretation of magnetotelluric sounding curves, *in* Geoelectric and geothermal studies: A. Adam, Ed., p. 165–221, Akademiai Kiado, Budapest.

Dey, A., and Morrison, H. F., 1979a, Resistivity modelling for arbitrarily shaped two-dimensional structures: Geophys. Prosp., v. 27, p. 106–136.

——— 1979b, Resistivity modeling for arbitrarily shaped three-dimensional structures: Geophysics, v. 44, p. 753–780.

Hermance, J. F., 1982a, The asymptotic response of three-dimensional basin offsets to magnetotelluric fields at long periods: The effects of current channeling: Geophysics, v. 47, p. 1562–1573.

——— 1982b, Refined finite-difference simulations using local integral forms: Application to telluric fields in two dimensions: Geophysics, v. 47, p. 825–831.

Hermance, J. F., and Thayer, R. E., 1975, The telluric-magnetotelluric method: Geophysics, v. 40, p. 664–668.

Hohmann, G. W., 1975, Three-dimensional induced polarization and electromagnetic modeling: Geophysics, v. 40, p. 309–324.

Jones, F. W., 1974, The perturbation of geomagnetic fields by two-dimensional and three-dimensional conductivity inhomogeneities: Pure and Appl. Geophys., v. 112, p. 793–800.

Jones, F. W., and Pascoe, L. J., 1972, The perturbation of alternating

geomagnetic fields by three-dimensional conductivity inhomogeneities: Geophys. J., v. 27, p. 479–485.
Mufti, I. R., 1976, Finite-difference resistivity modelling for arbitrarily shaped two-dimensional structures: Geophysics, v. 41, p. 62–78.
Raiche, A. P., 1974, An integral equation approach to three-dimensional modeling: Geophys. J., v. 36, p. 363–376.
Reddy, I. K., Rankin, D., and Phillips, R. J., 1977, Three-dimensional modeling in magnetotelluric and magnetic variational sounding: Geophys. J., v. 51, p. 313–325.
Stodt, J. A., Hohmann, G. W., and Ting, S. C., 1981, The telluric-magnetotelluric method in two- and three-dimensional environments: Geophysics, v. 46, p. 1137–1147.
Ting, S. C., and Hohmann, G. W., 1981, Integral equation modeling of three-dimensional magnetotelluric response: Geophysics, v. 46, p. 182–197.
Wannamaker, P. E., Ward, S. H., Hohmann, G. W., and Sill, W. R., 1980, Magnetotelluric models of the Roosevelt Hot Springs Thermal Area, Utah: Dept. Geol. and Geophys., Univ. Utah topical rep., contract no. DE-AC07-79ET27002, 213 p., Sept.
Weidelt, P., 1975, Electromagnetic induction in three-dimensional structures: J. Geophys., v. 41, p. 85–109.

APPENDIX
CALCULATING DERIVATIVES NEAR ELECTRICAL DISCONTINUITIES

The potential field U is a continuous function of space throughout the modeling domain. However, the normal derivatives of U are discontinuous across boundaries where σ is discontinuous. This poses a problem for numerically evaluating the components of the electric field intensity as the derivative of the electric potential ($\mathbf{E} = -\nabla U$) using methods which rely on simple central difference formulas. Recognizing that $\mathbf{E}$ may, in fact, be discontinuous at a node P (see Figure 3), one can evaluate the electric field in a vanishingly small region of the node P, but in one of the homogeneous prisms which abut at that point (Figure 2). Hence each electric field component can be evaluated in each of the four prisms, but vanishingly close to the central node P.

Upon considering the continuity of tangential electric field components across discontinuities, one has the following equalities:

$$E^P_{r1} = E^P_{r4}, E^P_{r2} = E^P_{r3}; E^P_{z1} = E^P_{z2}; E^P_{z3} = E^P_{z4};$$
$$E^P_{\theta 1} = E^P_{\theta 2} = E^P_{\theta 3} = E^P_{\theta 4}.$$

In addition, assuming that in each of the homogeneous subregions the potential can be expanded as a Taylor series, then, using the notation described in the text, the potentials at the right-hand node R and the left-hand node L, respectively, are related to the potential at the central node through

$$U_R = U_p + d_R\,\partial U_1/\partial r + (d_R^2/2)\partial^2 U_1/\partial r^2 \qquad (A-1)$$

and

$$U_L = U_p - d_L\,\partial u_2/\partial r + (d_L^2/2)\partial^2 U_2/\partial r^2. \qquad (A-2)$$

The expressions (A–1) and (A–2) can be rewritten in the forms

$$\partial U_1/\partial r = (U_R - U_p)/d_R - (d_R/2)\partial^2 U_1/\partial r^2, \quad (A-3)$$

and

$$\partial U_2/\partial r = (U_p - U_L)/d_L + (d_L/2)\partial^2 U_2/\partial r^2. \quad (A-4)$$

The interpretation of each of these expressions, respectively, is that $\partial U_1/\partial r$ is the radial derivative of U in medium 1 immediately adjacent and vanishingly close to the central node P, whereas $\partial U_2/\partial r$ is the radial derivative of U immediately adjacent to P in medium 2. If the conductivity is the same in both media, then of course $\partial U_1/\partial r = \partial U_2/\partial r$.

We now algebraically manipulate equations (A–3) and (A–4) to eliminate the continuous second derivatives on the right-hand side of these expressions. Using Laplace's equation $\nabla^2 U = 0$, we can write

$$\partial^2 U_j/\partial r^2 = -(1/r)\partial U_j/\partial r - (1/r^2)\partial^2 U_j/\partial\theta^2 - \partial^2 U_j/\partial z^2, \qquad (A-5)$$

where j is the index corresponding to each medium, 1 or 2. This expression can be substituted into the right-hand side of equations (A–3) and (A–4) which can be factored into the forms

$$[1 - (d_R/2r)]\partial U_1/\partial r = (U_R - U_p)/d_R + (d_R/2)[(1/r^2)\partial^2 U_1/\partial\theta^2 + \partial^2 U_1/\partial z^2], \qquad (A-6)$$

and

$$[1 + (d_L/2r)]\partial U_2/\partial r = (U_p - U_L)/d_L - (d_L/2)[(1/r^2)\partial^2 U_2/\partial\theta^2 + \partial^2 U_2/\partial z^2]. \qquad (A-7)$$

Expression (A–7) can be factored into an expression for $[(1/r^2)\partial^2 U_2/\partial\theta^2 + \partial^2 U_2/\partial z^2]$ which, because of the continuity of the potential along the 1-2 interface, is equal to $[(1/r^2)\partial^2 U_1/\partial\theta^2 + \partial^2 U_1/\partial z^2]$ in expression (A–6), and can be substituted for the latter terms. Recognizing also, because of the continuity of normal current flow across the vertical interface through the nodal point P, that

$$\partial U_2/\partial r = [(\sigma_1 + \sigma_4)/(\sigma_2 + \sigma_3)]\partial U_1/\partial r, \qquad (A-8)$$

expressions (A–6) and (A–7) can be combined to provide the forms for the derivatives $\partial U_1/\partial r$ and $\partial U_2/\partial r$. These in turn lead to the following expressions for the electric field components:

$$E^P_{r1} = E^P_{r4} = -(\sigma_2 + \sigma_3)[(d_L/d_R)(U_R - U_p) + (d_R/d_L)(U_p - U_L)] \cdot \{[d_L - (d_R d_L/2r)](\sigma_2 + \sigma_3) + [d_R + (d_R d_L/2r)](\sigma_1 + \sigma_4)\}^{-1}, \qquad (A-9)$$

and

$$E^P_{r2} = E^P_{r3} = -(\sigma_1 + \sigma_4)[(d_L/d_R)(U_R - U_p) + (d_R/d_L)(U_P - U_L)] \cdot \{[d_L - (d_r d_L/2r)](\sigma_2 + \sigma_3) + [d_R + d_L/2r)](\sigma_1 + \sigma_4)\}^{-1}. \qquad (A-10)$$

One can readily see that these two expressions differ by the ratio $(\sigma_2 + \sigma_3)$: $(\sigma_1 + \sigma_4)$, as they should according to equation (A–8). Relations (A–9) and (A–10) provide the finite-difference expressions needed to calculate the radial components of the electric field on either side of an electrical discontinuity. When the medium is homogeneous (i. e., when $\sigma_1 = \sigma_2 = \sigma_3 = \sigma_4$), these expressions are equal to each other and can be represented by the usual central diffference formula.

Similar considerations lead to expressions for the vertical electric field component E_z.

The derivation parallels the above development and is not reproduced here. The resulting expressions for the vertical electric field components are

$$E^P_{z1} = E^P_{z2} = -(\sigma_3 + \sigma_4)[(d_U/d_D)(U_D - U_P) - (d_D/d_U)(U_P - U_U)] \cdot [d_D(\sigma_1 + \sigma_2) + d_U(\sigma_3 + \sigma_4)]^{-1}, \qquad (A-11)$$

and

$$E^P_{z3} = E^P_{z4} = -(\sigma_1 + \sigma_2)[(d_U/d_D)(U_D - U_P) - (d_D/d_U)(U_P - U_U)] \cdot [d_D(\sigma_1 + \sigma_2) + d_U(\sigma_3 + \sigma_4)]^{-1}. \qquad (A-12)$$

It is clear that the ratio of equation (A–11) to equation (A–12) is given by $(\sigma_3 + \sigma_4)$:$(\sigma_1 + \sigma_2)$.